Nano Research
2024, 17(4): 3217–3223

ISSN 1998-0124 CN 11-5974/O4
https://doi.org/10.1007/s12274-023-6114-z

Research Article

# Synthesis of uniform two-dimensional $MoS_2$ films via thermal evaporation

Xue-Wei Lu (✉), Zhewei Li, Chen-Kai Yang, Weijia Mou, and Liying Jiao (✉)

*Key Laboratory of Organic Optoelectronics and Molecular Engineering of the Ministry of Education, Department of Chemistry, Tsinghua University, Beijing 100084, China*



**Received:** 3 July 2023 / **Revised:** 17 August 2023 / **Accepted:** 20 August 2023

## ABSTRACT

Two-dimensional (2D) molybdenum disulfide ($MoS_2$) holds great potential for various applications such as electronic devices, catalysis, lubrication, anti-corrosion and so on. Thermal evaporation is a versatile thin film deposition technique, however, the conventional thermal evaporation techniques face challenges in producing uniform thin films of $MoS_2$ due to its high melting temperature of 1375 °C. As a result, only thick and rough $MoS_2$ films can be obtained using these methods. To address this issue, we have designed a vacuum thermal evaporation system specifically for large-scale preparation of $MoS_2$ thin films. By using $K_2MoS_4$ as the precursor, we achieved reliable deposition of uniform polycrystalline $MoS_2$ thin films with a size of 50 mm × 50 mm and controllable thickness ranging from 0.8 to 2.4 nm. This approach also allows for patterned deposition of $MoS_2$ using shadow masks and sequential deposition of $MoS_2$ and tungsten disulfide ($WS_2$), similar to conventional thermal evaporation techniques. Moreover, we have demonstrated the potential applications of the obtained $MoS_2$ thin films in field effect transistors (FETs), memristors and electrocatalysts for hydrogen evolution reaction (HER).

## KEYWORDS

thermal evaporation, molybdenum disulfide, two-dimensional, memristors, hydrogen evolution reaction

## 1 Introduction

Two-dimensional (2D) transition metal dichalcogenides (TMDCs) thin films, such as molybdenum disulfide ($MoS_2$) have sparked tremendous research interest owing to their promising applications in electronics [1, 2], optoelectronics [3], lubrication [4], catalysis [5–7], anti-corrosion [8, 9] and so on. Chemical vapor deposition (CVD) has proved to be a successful method for synthesizing high quality 2D $MoS_2$ and other TMDCs on various substrates [10]. However, most of the CVD growth of 2D $MoS_2$ has been carried out in horizontal tube furnaces, which significantly limited the size of the resulting films and the scalability of the growth process. Compared to CVD growth in tube furnaces, thermal evaporation offers several advantages. Firstly, it allows for the production of highly uniform thin films over large areas. Secondly, it provides reliable control over the deposition rate and thickness of the films. Additionally, thermal evaporation enables patterned deposition using masks and the deposition of alternative materials. These advantages make thermal evaporation a desirable method for the fabrication of 2D films, such as $MoS_2$. However, the high melting temperature of $MoS_2$ (1375 °C) poses a significant challenge in achieving uniform thin films through conventional thermal evaporation techniques. Previous attempts have resulted in the production of thick (~ 250 nm) and rough $MoS_2$ films with nanosphere morphology [11–13].

To address this challenge, we designed a vacuum thermal evaporation system for the preparation of 2D $MoS_2$ thin films. The large, vertical chamber and a face-to-face precursor supply configuration together with a rotatable sample holder allowed for the large area and uniform deposition of 2D $MoS_2$ thin films with a size of up to 50 mm × 50 mm. By optimizing the parameters such as the amount of precursors, deposition time, and the distance between substrates and precursors, we were able to achieve precise control over the thickness of $MoS_2$ thin films, ranging from 0.8 to 2.4 nm. Similar to conventional thermal deposition of metals, we also achieved the patterned deposition of $MoS_2$ with a shadow mask and the layer by layer deposition of $MoS_2$ and tungsten disulfide ($WS_2$). In addition to planar substrates, the thermal deposition of $MoS_2$ can also be performed on curved substrates, such as carbon cloth. Field-effect transistors (FETs) fabricated on the obtained 2D $MoS_2$ thin films exhibited on/off current ratios on the order of $10^5$. Besides FETs, these samples are also suitable for fabricating memristors and catalysts for hydrogen evolution reaction (HER). Our work demonstrates the great potential of thermal evaporation technique in the preparation of uniform 2D $MoS_2$ thin films with large area and controllable thickness.

## 2 Results and discussion

The thermal deposition of $MoS_2$ thin films was conducted in a homemade vacuum thermal evaporation system as schematically shown in Fig. 1(a). To achieve the large area and uniform deposition of 2D $MoS_2$, the sample holder and the heating stage were vertically mounted in a large chamber (~ 27 $dm^3$) to ensure the uniform diffusion of gas phase precursors [14]. Additionally, the sample holder was designed to be rotatable, further enhancing

Address correspondence to Xue-Wei Lu, luxuewei@mail.tsinghua.edu.cn; Liying Jiao, lyjiao@mail.tsinghua.edu.cn

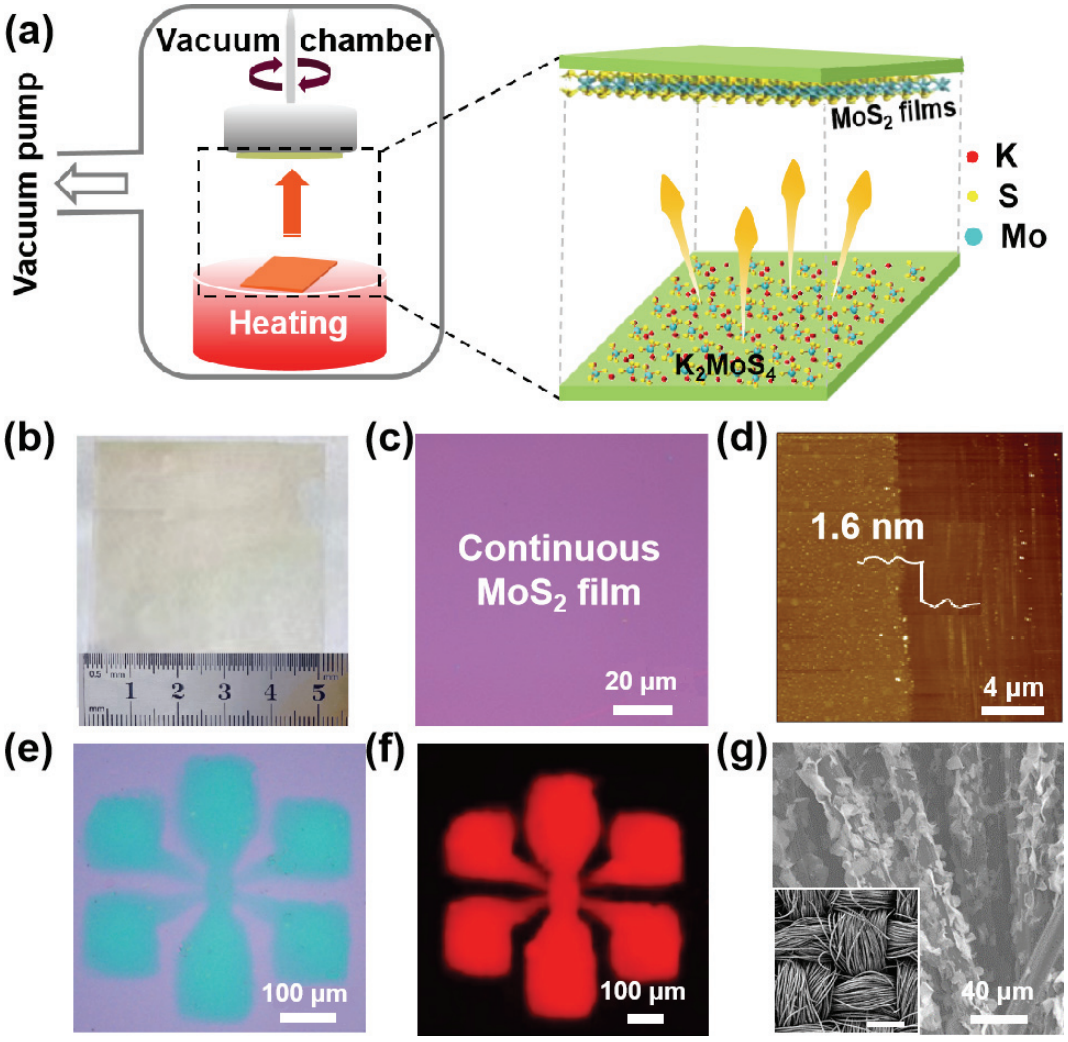


**Figure 1** Thermal deposition of $MoS_2$ thin films in our homemade thermal evaporation system. (a) Schematic of the set-up used for the deposition of $MoS_2$ thin films. (b) Photograph showing a bilayer $MoS_2$ film grown on a mica substrate. (c) Optical image of the bilayer $MoS_2$ thin film transferred to a $SiO_2$/Si substrate, exhibiting uniform contrast indicative of homogeneous thickness. (d) AFM image of the bilayer $MoS_2$ thin film with a thickness of ~ 1.6 nm. (e) Optical image of a $MoS_2$ pattern transferred to a $SiO_2$/Si substrate. (f) Raman mapping image of the patterned $MoS_2$, demonstrating the uniformity of the deposited material. (g) SEM image of the $MoS_2$ flakes grown on carbon cloth. Inset: the low-magnification SEM image of the carbon cloth. Scale bar: 1 mm (inset of (g)).

the uniformity of precursor distribution between the source and growth substrates. The optimal rotational speed of the sample holder was set at tens of revolutions per minute (RPM). To lower the deposition temperature of $MoS_2$, we utilized potassium tetrathiomolybdate ($K_2MoS_4$), which decomposes into $MoS_2$ at 600 °C, as the $MoS_2$ source, as shown in the following reaction equation [15]

$$K_2MoS_4 \xrightarrow{600\ ^\circ C} MoS_2 + K_2S + S$$

To further improve the uniformity of $MoS_2$ supply, $K_2MoS_4$ was uniformly dispersed on a mica substrate of the same size as the growth substrate, allowing for face-to-face source supply (Fig. S1 in the Electronic Supplementary Material (ESM)). The precise control of $MoS_2$ thin film thickness was achieved by adjusting the amount of precursors, deposition time, and the distance between the growth substrates and precursors. The resulting $MoS_2$ films had thicknesses of approximately 0.8, 1.6, and 2.4 nm, corresponding to 1, 2, and 3 L, respectively (Fig. S2 in the ESM), and their surfaces were relatively smooth over the entire films (Fig. S7 in the ESM).

By optimizing growth conditions such as the amount of precursors, temperature, the selection of substrates (Fig. S3 in the ESM), we successfully obtained $MoS_2$ thin films with a large size of up to 50 mm × 50 mm on mica substrates. Specifically, for the deposition of bilayer $MoS_2$ thin films, a thermal deposition process was carried out at a heating temperature of 900 °C (with a substrate temperature of 600 °C) for 20 min using ~ 0.5 mg of $K_2MoS_4$ as the precursor. The distance between the substrate and the precursor was maintained at ~ 14 mm, while the chamber pressure during the deposition process was kept at around $10^{-3}$ mbar.

The $MoS_2$ thin films obtained through the thermal deposition process were subsequently transferred to a $SiO_2$/Si substrate using water-assisted peeling [5] for further characterization. The optical image of the sample revealed a uniform contrast, indicating a consistent thickness across the entire $MoS_2$ thin film (Fig. 1(c)). Atomic force microscopy (AFM) measurements showed a film thickness of ~ 1.6 nm, confirming the bilayer structure of the $MoS_2$ film (Fig. 1(d)). Additionally, by adjusting the amount of the precursor and the deposition time, we were able to synthesize single-layer and trilayer $MoS_2$ films (Fig. S2 in the ESM).

The vertical deposition of $MoS_2$ in our approach enables the patterned deposition of $MoS_2$ using shadow masks (Fig. 1(e) and Fig. S4 in the ESM). The Raman mapping image of the transferred $MoS_2$ (Fig. 1(f)) confirms the uniformity of the $MoS_2$ pattern. We extended our approach to deposit thin films of other TMDCs. A $WS_2$ thin film with a thickness of ~ 0.8 nm was successfully grown on a mica substrate using the same deposition method and subsequently transferred to a $SiO_2$/Si substrate (Fig. S6(a) in the

ESM). Additionally, by employing this technique, we obtained $MoS_2$-$WS_2$ vertical heterojunction by sequentially depositing $MoS_2$ and $WS_2$ on a mica substrate, followed by transfer onto a $SiO_2$/Si substrate (Fig. S6(b) in the ESM). The presence of distinct Raman peaks corresponding to $MoS_2$ (383.7 and 405.3 $cm^{-1}$) and $WS_2$ (350.5 and 417.5 $cm^{-1}$) confirmed the successful formation of $MoS_2$-$WS_2$ vertical heterojunction (Fig. S6(c) in the ESM). In addition to planar substrates, carbon cloth was also used as the substrate for the deposition of $MoS_2$. The scanning electron microscope (SEM) image of the $MoS_2$ deposited on carbon cloth clearly showed the morphology of the as-deposited $MoS_2$ flakes (Fig. 1(g)). These flakes exhibited an average size of tens of micrometers and a thickness in the nanometer range.

To investigate the crystallinity of the obtained $MoS_2$ films, we imaged the obtained samples with transmission electron microscope (TEM) by transferring the obtained $MoS_2$ samples to holey carbon TEM grids via water-assisted peeling (Fig. 2(a)). The high-resolution TEM image revealed the hexagonal lattice of the obtained $MoS_2$ thin film (Fig. 2(b)). The selected-area electron diffraction (SAED) patterns acquired at two different positions of $MoS_2$ films with an aperture size of ~ 130 nm showed hexagonal symmetry for the $MoS_2$ structure (Figs. 2(c) and 2(d)). We also collected SAED patterns at multiple locations on the films and observed consistent hexagonal patterns with the same orientations. This indicates that the $MoS_2$ films possess a single crystalline domain size well above 130 nm, which is significantly larger than that of $MoS_2$ produced by the thermal evaporation technique (≤ 25 nm) as reported previously [11].

Raman spectroscopy was employed to characterize the as-deposited $MoS_2$ thin films. Two characteristic Raman peaks at 383.7 and 405.3 $cm^{-1}$ were observed on $MoS_2$ films which were assigned to the in-plane ($E^1_{2g}$) mode and the out-of-plane ($A_{1g}$) mode of $MoS_2$, respectively (Fig. 3(c)). The photoluminescence (PL) spectrum of $MoS_2$ thin films exhibited two peaks at ~ 625 and ~ 672 nm (Fig. 3(d)), which were similar to the values previously reported for bilayer and trilayer $MoS_2$ [16]. To evaluate the uniformity of $MoS_2$ thin films over a large area, we performed Raman line scan over a length of 10 mm with a step size of 0.8 μm, as shown in the Raman mapping image (Fig. 3(a)). The obtained $MoS_2$ thin films exhibited uniform peak intensities and frequency difference (~ 21.6 $cm^{-1}$), indicating the high uniformity of the films over a large area. Raman mapping was performed over an area of 35 μm × 40 μm and the Raman mapping image with the intensity of the $A_{1g}$ mode displayed a uniform color distribution. This observation also indicates the high spatial uniformity of the $MoS_2$ thin films (Fig. 3(b)).

To study the chemical state and elemental composition of the obtained $MoS_2$ thin films, X-ray photoelectron spectroscopy (XPS) was employed for surface analysis. According to the XPS data, the Mo $3d_{5/2}$ (~ 229.9 eV) and Mo $3d_{3/2}$ (~ 233.0 eV) peaks were in line with $Mo^{4+}$ (Fig. 3(e)), and S $2p_{3/2}$ (~ 162.5 eV) and S $2p_{1/2}$ (~ 163.7 eV) peaks were assigned to $S^{2-}$ (Fig. 3(f)). The binding energies for both Mo and S elements measured on the obtained samples with XPS were in agreement with the values of $MoS_2$ in 2H phase [17, 18]. The atomic ratio of Mo:S was estimated to be ~ 1:2, and no $K^+$ was detected on the water-rinsed $MoS_2$ thin films, providing further evidence of the high purity of the obtained $MoS_2$ thin films.

To evaluate the electrical performance of the as-grown $MoS_2$ films, large arrays of back-gated FETs were fabricated on $MoS_2$ thin films transferred on 300 nm $SiO_2$/Si substrates with 10 nm In/50 nm Au as source and drain electrodes by electron beam lithography (EBL). The electrical measurement was performed at room temperature in vacuum (~ $10^{-5}$ mbar), and the transfer characteristic of the obtained $MoS_2$ thin films exhibited intrinsic n-type conduction with an on/off current ratio of ~ $10^5$ (Figs. 4(a) and 4(b)). We measured 12 $MoS_2$ FETs with a channel length of 10 μm and a channel width of 100 μm and the estimated on/off current ratios and mobility were within the range of $10^4$–$10^5$ and 0.01–0.05 $cm^2 \cdot V^{-1} \cdot s^{-1}$, respectively (Fig. S5 in the ESM). The measured electrical performance of our $MoS_2$ thin films was comparable to that of polycrystalline $MoS_2$ prepared by the room temperature magnetron sputtering and laser annealing [19].

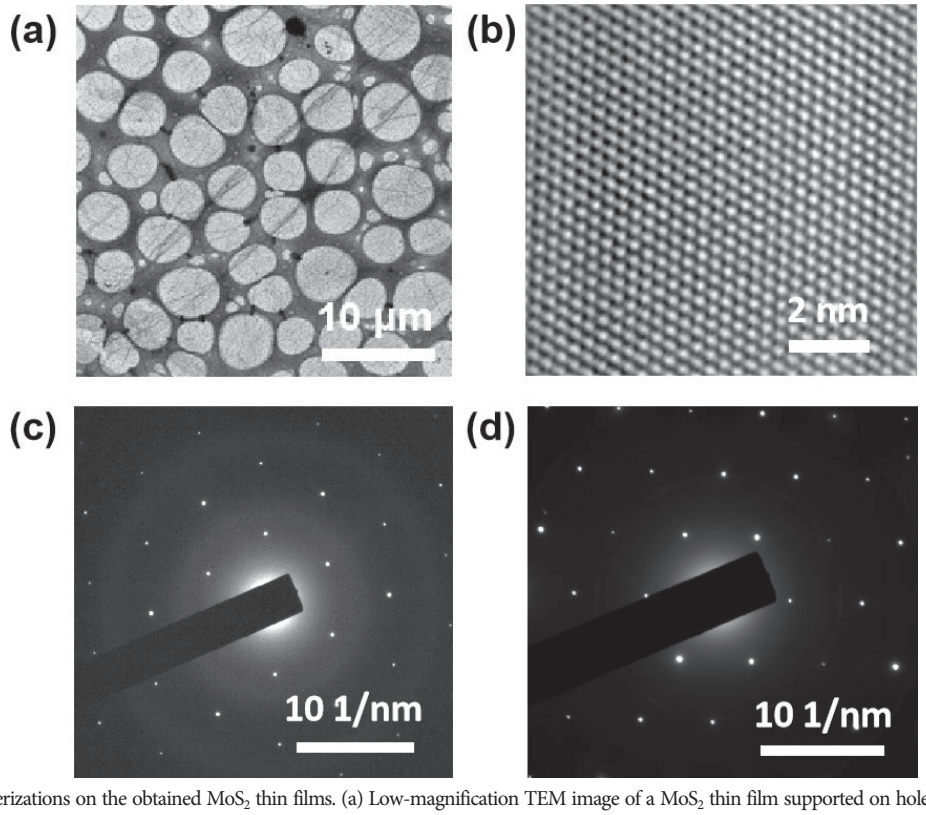


**Figure 2** TEM characterizations on the obtained $MoS_2$ thin films. (a) Low-magnification TEM image of a $MoS_2$ thin film supported on holey carbon grid. (b) High-resolution TEM image of the $MoS_2$ thin film, showing hexagonal lattice. (c) and (d) SAED patterns collected at different positions on the same $MoS_2$ film.

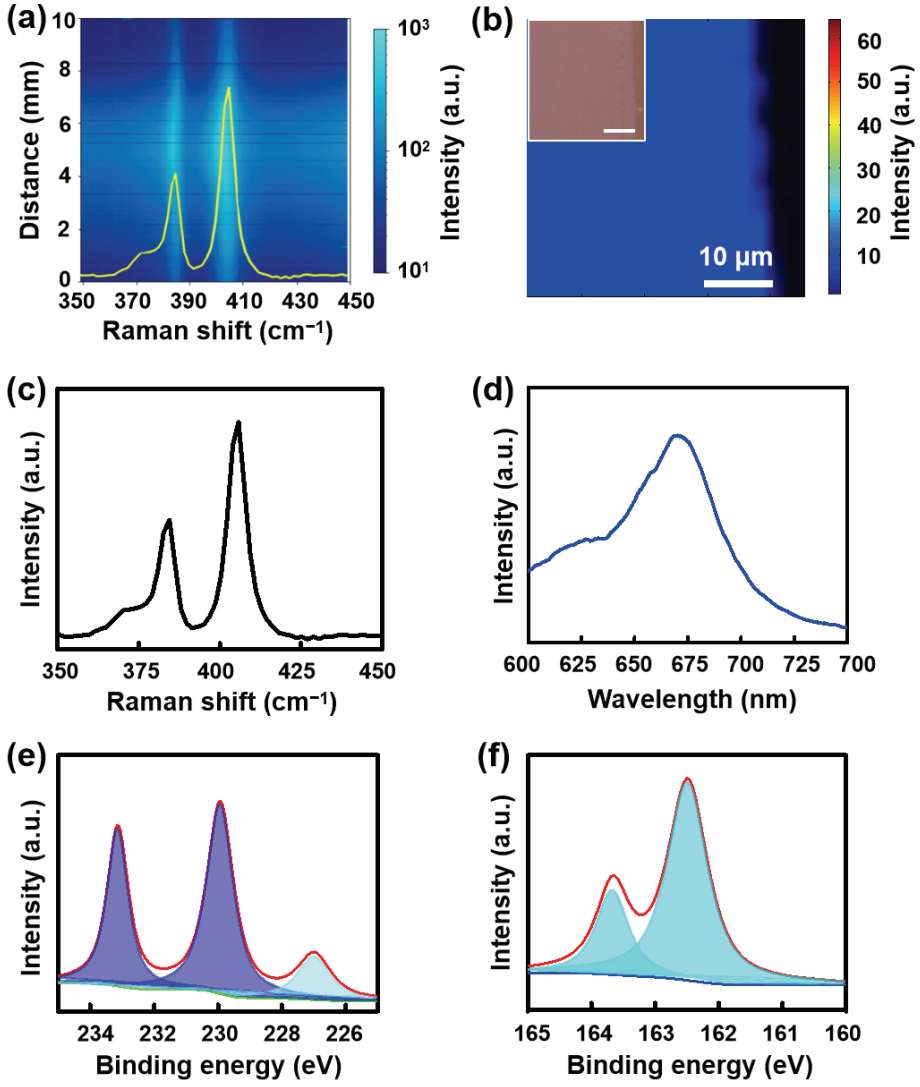


**Figure 3** Spectroscopic characterizations on the obtained $MoS_2$ thin films. (a) The Raman line scanning image plotted with the intensities of 383.7 $cm^{-1}$ ($E^1_{2g}$) and 405.3 $cm^{-1}$ ($A_{1g}$) over a length of 10 mm with a step size of 0.8 μm. (b) Raman area mapping image. (c) Raman and (d) PL spectra of the $MoS_2$ thin films shown in the inset of (b). Scale bar in the inset of (b): 10 μm. XPS spectra of (e) the Mo 3d core level and (f) the S 2p core level of the $MoS_2$ thin films.

The relatively low mobility of our polycrystalline $MoS_2$ indicates that this kind of sample exhibits a lot of grain boundaries, and such $MoS_2$ is suitable for memristors as conductive filaments are more likely to form along the grain boundaries [20]. We fabricated vertical-structured memristors (Fig. 4(c)), where $MoS_2$ thin films with thickness of ~ 1.6 nm were sandwiched between bottom electrodes of Au (50 nm) and top electrodes of Ag (50 nm). Both electrodes were patterned by EBL followed by thermal evaporation of metals. The mechanism of the memory operation is based on the formation and the rupture of the conductive Ag filament through the $MoS_2$ thin film. When the positive bias voltage is applied to the Ag electrode, a conductive Ag filament is formed, causing the memristor to switch from high resistance state (HRS) to low resistance state (LRS), and the Ag filament is ruptured during the switch from positive bias voltage to negative bias voltage, leading to the transition from LRS to HRS [21]. The active area of the device was defined by the width of both electrodes, which was approximately 5 μm × 5 μm in our devices. The current–voltage ($I$–$V$) characteristics of a typical memristor displayed bipolar non-volatile memory switching property at a set voltage ($V_{set}$) of ~ 0.70 V and a reset voltage ($V_{reset}$) of ~ −0.24 V at a sweep voltage range from −0.30 to 0.70 V under ambient conditions, as shown in Fig. 4(d). Note that here the compliance current in the positive bias region was set to 10 μA to prevent $MoS_2$ from being broken down. The as-made memristor was in a HRS for the $V$ sweep from 0 to 0.70 V (sweep 1) and changed to a LRS at ~ 0.70 V. The device maintained the LRS during the sweep from 0.70 to 0 V (sweep 2) and then reset to a HRS at ~ −0.24 V during the sweep from 0 to −0.30 V (sweep 3), and remained the HRS during the sweep from −0.24 to 0 V (sweep 4). The switching voltage we measured is lower than the values reported in most of the literature (0.10–10 V) [21, 22].

This kind of $MoS_2$ is not only suitable for memristors, but also appropriate for efficient electrocatalysts for HER as the grain boundaries can serve as active sites for HER catalysis [23, 24]. We measured the electrocatalytic HER properties of our $MoS_2$ grown on carbon cloth in 0.5 M $H_2SO_4$ electrolyte at room temperature via three-electrode setup. The $H_2$ evolution overpotential at 10 $mA{\cdot}cm^{-2}$ and the Tafel slope of our $MoS_2$ samples were estimated to be ~ 168 and ~ 78 $mV{\cdot}dec^{-1}$ (Figs. 4(e) and 4(f)), respectively, which were superior to the averaged values for 2H $MoS_2$ flakes (~ 200 and ~ 90 $mV{\cdot}dec^{-1}$, respectively) [25–28]. In addition to the enriched defects in our polycrystalline $MoS_2$, the formation of high-quality $MoS_2$-carbon cloth interfaces at a high temperature of 600 °C is advantageous for reducing contact resistance, leading to a relatively rapid charge transfer rate.

## 3 Conclusions

In summary, we designed a vacuum thermal evaporation system

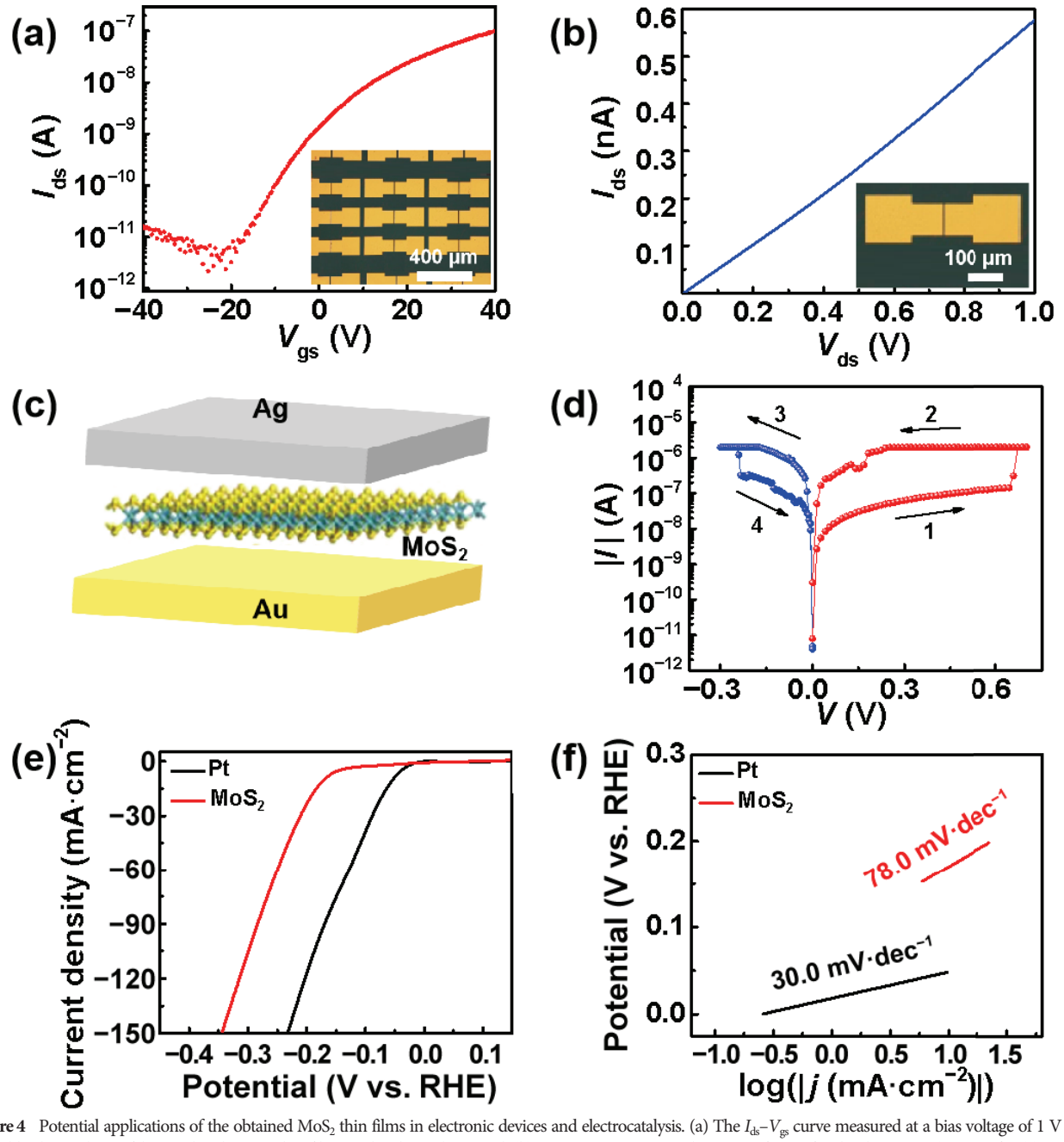


**Figure 4** Potential applications of the obtained $MoS_2$ thin films in electronic devices and electrocatalysis. (a) The $I_{ds}$–$V_{gs}$ curve measured at a bias voltage of 1 V for a typical back-gated FET fabricated with $MoS_2$ thin films as the channel material. (b) $I_{ds}$–$V_{ds}$ curve measured at a $V_{gs}$ of 40 V for the device in (a). Insets for (a) and (b): the optical images of an array of back-gated FETs and an individual FET, respectively. (c) Schematics for the $MoS_2$ memristor. (d) The $I$–$V$ curve of a $MoS_2$ memristor measured under voltages between −0.30 and 0.70 V. The gate voltage was 0 V. The direction of the voltage sweeps 1–4 was indicated by the arrows. The sweep rate was 200 mV·s$^{-1}$. (e) HER polarization curves for Pt and $MoS_2$ flakes grown on carbon cloth. (f) Tafel plots for Pt and $MoS_2$ flakes grown on carbon cloth.

for the large-scale preparation of 2D $MoS_2$ thin films. This homemade system allowed us to achieve highly uniform deposition of $MoS_2$ thin films over a large area, precise control over film thickness, patterned deposition, and sequential deposition of different materials. We obtained 1–3 layer polycrystalline $MoS_2$ thin films with a size of 50 mm × 50 mm and a single crystalline domain size exceeding 130 nm. In addition to $MoS_2$, 2D $WS_2$ thin films and $MoS_2$-$WS_2$ vertical heterojunction were also obtained using this method, demonstrating its universality. We further applied the obtained $MoS_2$ thin films in electronic devices and electrocatalysts for HER. The as-deposited $MoS_2$ based vertical-structured memristor showed a lower switching voltage of ~ 0.70 V compared to other $MoS_2$ based memristors in most of previous reports. The HER overpotential at 10 mA·cm$^{-2}$ of $MoS_2$ flakes deposited on carbon cloth was measured to be about 168 mV, which was superior to the averaged values for 2H $MoS_2$ flakes reported previously. Our work not only opens up a new avenue for the large-scale and controllable synthesis of $MoS_2$ thin films by thermal evaporation technique but also demonstrates the potential applications of the obtained $MoS_2$ thin films in FETs, memristors and electrocatalysts.

## 4 Experimental section

### 4.1 Synthesis of $K_2MoS_4$ precursor

The solid precursor $K_2MoS_4$ was prepared following previously published method [29]. 1 g of ammonium tetrathiomolybdate $(NH_4)_2MoS_4$ (Sigma-Aldrich, powders, purity 99.9%) was dissolved in 10 mL of 2 M potassium hydroxide (Sigma-Aldrich, flakes, purity 81%) aqueous solution. The $NH_3$ produced during the synthetic reaction was evacuated by vacuum pumping for 20

h. A solution that contains $K^+$ and $MoS_4^{2-}$ ions was obtained after the removal of $NH_3$. Then 20 mL ethanol was added to the above solution to precipitate $K_2MoS_4$. The obtained precipitation was thoroughly rinsed with ethanol to completely remove the possible KOH residue and then was freeze-dried and stored under vacuum.

### 4.2 Thermal deposition of 2D $MoS_2$ thin films

Thermal deposition of $MoS_2$ thin films was conducted in a homemade vacuum thermal evaporation system. To ensure the spatial uniformity of the precursor, we adopted a face-to-face precursors supply configuration (Fig. S1 in the ESM). The precursor $K_2MoS_4$ was uniformly dispersed on a mica substrate which was placed in the center of the heating stage. A freshly-cleaved mica substrate was fixed on the sample holder, which was placed face to face with the mica loaded with $K_2MoS_4$ precursor. Note that the distance between the substrate and the precursor was adjustable within a range of 7–180 mm, and the appropriate distance between them was ~ 14 mm for the thermal deposition of $MoS_2$ thin films. Before deposition, the chamber was evacuated by a turbo pump to reach a vacuum pressure of ~ $10^{-5}$ mbar at 25 °C. Then the furnace was heated to the temperature of 800–1000 °C with a heating rate of 20 °C·min$^{-1}$ and kept there for 10–30 min for the thermal deposition of $MoS_2$ films, followed by cooling down to room temperature naturally. During the thermal deposition process, the temperature at the growth substrate was in the range of 450–650 °C, and the pressure in the furnace was on the order of $10^{-5}$–$10^{-3}$ mbar, which depended on the amount of the precursor and the temperature.

### 4.3 Transfer of 2D $MoS_2$ films

A poly (methylmethacrylate) (PMMA)-mediated transfer approach was used to transfer the as-grown 2D $MoS_2$ thin films to $SiO_2$/Si substrates and holey carbon grids for device fabrication and TEM characterization, respectively. First, a PMMA (AR-P679.04) thin film was spin-coated (3000 r.p.m., 1 min) onto a mica substrate covered with 2D $MoS_2$ films and backed at ~ 100 °C for 10 min. Then, the baked sample was soaked in deionized water at room temperature to allow for the water-assisted peeling of the PMMA film and underlying 2D $MoS_2$ films from the mica substrate. Next, the PMMA film with 2D $MoS_2$ thin films was attached immediately to the target substrate and dried in air. Finally, the PMMA film was removed by hot acetone.

### 4.4 Characterizations on the obtained 2D $MoS_2$ films

Optical images were captured with an Olympus BX 51M microscope. Raman and PL spectra were collected with a Horiba-Jobin-Yvon Raman system under 532 nm laser excitation at a power of 2 mW. The Raman mapping images were collected with a step of 0.8 μm. The Si peak at 520.7 cm$^{-1}$ was used for calibration in the data analysis. AFM images were taken with a Bruker Dimension Icon in tapping mode. XPS measurements were performed with an ESCALAB 250Xi system using Al K$\alpha$ as the excitation source. All binding energies were referenced to the C 1s peak at 284.8 eV. SEM images were taken with the SEM system (JEOL JSM-7900F) at 5 kV. TEM images and SAED patterns were acquired with a JEOL JEM 2100 and a FEI Tecnai G20 at 200 kV.

### 4.5 Devices fabrication and measurement

2D $MoS_2$ films were transferred to $SiO_2$/Si substrates for device fabrications and electrical measurements. Source and drain electrodes were fabricated on 2D $MoS_2$ thin films by EBL followed by thermal evaporation of metals (10 nm In and 50 nm Au) and lift-off. The obtained FETs were measured using a four-probe station with Agilent B1500 A at room temperature under high vacuum ($10^{-5}$ mbar). The carrier mobility of FETs was estimated using the equation below

$$\mu = \frac{L}{W \times (\varepsilon_0 \varepsilon_r / d) V_{ds}} \times \frac{dI_{ds}}{dV_{gs}}$$

where $L$ and $W$ represent length and width of the channel, respectively; $\varepsilon_0$ and $\varepsilon_r$ represent vacuum permittivity and relative permittivity, respectively; $d$ is the thickness of the dielectric layer; $I_{ds}$, $V_{ds}$ and $V_{gs}$ represent source-drain current, source-drain voltage and gate voltage, respectively.

The fabrication of memristors was as follows. The bottom electrode was fabricated on $SiO_2$/Si substrates by EBL followed by thermal evaporation of metals (10 nm In and 50 nm Au) and lift-off. Then, the obtained bottom electrode was covered by transferred $MoS_2$ thin films. Finally, a top electrode was fabricated by EBL followed by thermal evaporation of Ag (50 nm) and lift-off in hot acetone. The memory operations were measured using a four-probe station with Agilent B1500 A.

### 4.6 Electrochemical measurements

All the electrochemical measurements were conducted with an electrochemical workstation (CHI660E). The HER was performed in 0.5 M $H_2SO_4$ solution using a three-electrode system with a saturated calomel electrode (SCE) as the reference electrode, a graphite rod as the counter electrode, and the carbon cloth covered by $MoS_2$ flakes as the working electrode. The effective surface area of $MoS_2$ flakes on carbon cloth was estimated to be ~ 50 mm$^2$. The polarization curves were recorded by linear sweep voltammetry (LSV) at a scan rate of 5 mV·s$^{-1}$ from −0.10 to −0.70 V versus the reference electrode. The reference electrode was calibrated against the reversible hydrogen electrode (RHE). All the potentials reported in our work were converted according to $E$ (vs. RHE) = $E$ (vs. SCE) + 0.2415 V. The current density was calculated by normalizing the surface area exposed to the electrolyte solution.

## Acknowledgements

This work was supported by the National Natural Science Foundation of China (No. 22105114), China Postdoctoral Science Foundation (No. 2020TQ0163), Tsinghua-Toyota Joint Research Fund and Tsinghua-Jiangyin Innovation Special Fund (No. 2022JYTH01).

**Electronic Supplementary Material:** Supplementary material (for the set-up of a vacuum thermal evaporation system for the deposition of 2D $MoS_2$ thin films, the face-to-face precursor supply configuration and more data on the obtained $MoS_2$ thin films) is available in the online version of this article at https://doi.org/10.1007/s12274-023-6114-z.

## References

[1] Wu, F.; Tian, H.; Shen, Y.; Hou, Z.; Ren, J.; Gou, G. Y.; Sun, Y. B.; Yang, Y.; Ren, T. L. Vertical $MoS_2$ transistors with sub-1-nm gate lengths. *Nature* **2022**, *603*, 259–264.

[2] Zheng, L.; Wang, X. W.; Jiang, H. J.; Xu, M. Z.; Huang, W.; Liu, Z. Recent progress of flexible electronics by 2D transition metal dichalcogenides. *Nano Res.* **2021**, *15*, 2413–2432.

[3] Choi, M.; Bae, S. R.; Hu, L.; Hoang, A. T.; Kim, S. Y.; Ahn, J. H. Full-color active-matrix organic light-emitting diode display on human skin based on a large-area $MoS_2$ backplane. *Sci. Adv.* **2020**, *6*, eabb5898.

[4] Zhang, J. Y.; Jiang, D.; Wang, D. S.; Yu, Q. L.; Bai, Y. Y.; Cai, M. R.; Weng, L. J.; Zhou, F.; Liu, W. M. $MoS_2$ lubricating film meets supramolecular gel: A novel composite lubricating system for space

applications. *ACS Appl. Mater. Interfaces* **2021**, *13*, 58036–58047.
[5] Liu, L. N.; Wu, J. X.; Wu, L. Y.; Ye, M.; Liu, X. Z.; Wang, Q.; Hou, S. Y.; Lu, P. F.; Sun, L. F.; Zheng, J. Y. et al. Phase-selective synthesis of 1T′ $MoS_2$ monolayers and heterophase bilayers. *Nat. Mater.* **2018**, *17*, 1108–1114.
[6] Liu, M. M.; Zhang, C. Y.; Han, A. L.; Wang, L.; Sun, Y. J.; Zhu, C. N.; Li, R.; Ye, S. Modulation of morphology and electronic structure on $MoS_2$-based electrocatalysts for water splitting. *Nano Res.* **2022**, *15*, 6862–6887.
[7] Niu, S. W.; Cai, J. Y.; Wang, G. M. Two-dimensional $MoS_2$ for hydrogen evolution reaction catalysis: The electronic structure regulation. *Nano Res.* **2020**, *14*, 1985–2002.
[8] Aleithan, S. H.; Al-Amer, K.; Alabbad, Z. H.; Khalaf, M. M.; Alam, K.; Alhashem, Z.; Abd El-Lateef, H. M. Highly scalable synthesis of $MoS_2$ thin films for carbon steel coatings: Influence of synthetic route on the nanostructure and corrosion performance. *J. Mater. Res. Technol.* **2023**, *23*, 1239–1251.
[9] Joseph, A.; Vijayan, A. S.; Shebeeb, C. M.; Akshay, K. S.; John Mathew, K. P.; Sajith, V. A review on tailoring the corrosion and oxidation properties of $MoS_2$-based coatings. *J. Mater. Chem. A* **2023**, *11*, 3172–3209.
[10] Liu, M. J.; Liao, J.; Liu, Y.; Li, L. Y.; Wen, R. J.; Hou, T. Y.; Ji, R.; Wang, K. L.; Xing, Z. G.; Zheng, D. et al. Periodical ripening for MOCVD growth of large 2D transition metal dichalcogenide domains. *Adv. Funct. Mater.* **2023**, *33*, 2212773.
[11] Abdullah, N.; Muzakir, S. K.; Shaafi, N. F.; Abdul Kadir, M. Z.; Mohamed, R. Characterizations of $MoS_2$ nanosphere fabricated using vacuum thermal evaporation at steady and rapid heating. *Mater. Today: Proc.* **2023**, *75*, 10–15.
[12] Balendhran, S.; Ou, J. Z.; Bhaskaran, M.; Sriram, S.; Ippolito, S.; Vasic, Z.; Kats, E.; Bhargava, S.; Zhuiykov, S.; Kalantar-Zadeh, K. Atomically thin layers of $MoS_2$ via a two step thermal evaporation-exfoliation method. *Nanoscale* **2012**, *4*, 461–466.
[13] Sivarajan, S.; Padmanabhan, R. Characterization of thermally evaporated $MoS_2$ thin film coatings. *Mater. Today: Proc.* **2016**, *3*, 2532–2536.
[14] Tang, L.; Li, T.; Luo, Y. T.; Feng, S. M.; Cai, Z. Y.; Zhang, H.; Liu, B. L.; Cheng, H. M. Vertical chemical vapor deposition growth of highly uniform 2D transition metal dichalcogenides. *ACS Nano* **2020**, *14*, 4646–4653.
[15] Barreau, N.; Bernède, J. C. $MoS_2$ textured films grown on glass substrates through sodium sulfide based compounds. *J. Phys. D: Appl. Phys.* **2002**, *35*, 1197–1204.
[16] Zhou, H. Q.; Yu, F.; Liu, Y. Y.; Zou, X. L.; Cong, C. X.; Qiu, C. Y.; Yu, T.; Yan, Z.; Shen, X. N.; Sun, L. F. et al. Thickness-dependent patterning of $MoS_2$ sheets with well-oriented triangular pits by heating in air. *Nano Res.* **2013**, *6*, 703–711.
[17] Baker, M. A.; Gilmore, R.; Lenardi, C.; Gissler, W. XPS investigation of preferential sputtering of S from $MoS_2$ and determination of $MoS_x$ stoichiometry from Mo and S peak positions. *Appl. Surf. Sci.* **1999**, *150*, 255–262.
[18] Voiry, D.; Mohite, A.; Chhowalla, M. Phase engineering of transition metal dichalcogenides. *Chem. Soc. Rev.* **2015**, *44*, 2702–2712.
[19] Sirota, B.; Glavin, N.; Voevodin, A. A. Room temperature magnetron sputtering and laser annealing of ultrathin $MoS_2$ for flexible transistors. *Vacuum* **2019**, *160*, 133–138.
[20] Xu, R. J.; Jang, H.; Lee, M. H.; Amanov, D.; Cho, Y.; Kim, H.; Park, S.; Shin, H. J.; Ham, D. Vertical $MoS_2$ double-layer memristor with electrochemical metallization as an atomic-scale synapse with switching thresholds approaching 100 mV. *Nano Lett.* **2019**, *19*, 2411–2417.
[21] Naqi, M.; Kang, M. S.; Liu, N.; Kim, T.; Baek, S.; Bala, A.; Moon, C.; Park, J.; Kim, S. Multilevel artificial electronic synaptic device of direct grown robust $MoS_2$ based memristor array for in-memory deep neural network. *npj 2D Mater. Appl.* **2022**, *6*, 53.
[22] Pi, S.; Li, C.; Jiang, H.; Xia, W. W.; Xin, H. L.; Yang, J. J.; Xia, Q. F. Memristor crossbar arrays with 6-nm half-pitch and 2-nm critical dimension. *Nat. Nanotechnol.* **2019**, *14*, 35–39.
[23] Xie, J. F.; Qu, H. C.; Xin, J. P.; Zhang, X. X.; Cui, G. W.; Zhang, X. D.; Bao, J.; Tang, B.; Xie, Y. Defect-rich $MoS_2$ nanowall catalyst for efficient hydrogen evolution reaction. *Nano Res.* **2017**, *10*, 1178–1188.
[24] Xie, J. F.; Zhang, H.; Li, S.; Wang, R. X.; Sun, X.; Zhou, M.; Zhou, J. F.; Lou, X. W.; Xie, Y. Defect-rich $MoS_2$ ultrathin nanosheets with additional active edge sites for enhanced electrocatalytic hydrogen evolution. *Adv. Mater.* **2013**, *25*, 5807–5813.
[25] Deng, S. J.; Luo, M.; Ai, C. Z.; Zhang, Y.; Liu, B.; Huang, L.; Jiang, Z.; Zhang, Q. H.; Gu, L.; Lin, S. W. et al. Synergistic doping and intercalation: Realizing deep phase modulation on $MoS_2$ arrays for high-efficiency hydrogen evolution reaction. *Angew. Chem., Int. Ed.* **2019**, *58*, 16289–16296.
[26] Gong, J.; Zhang, Z. Y.; Zeng, Z. P.; Wang, W. J.; Kong, L. X.; Liu, J. Y.; Chen, P. Graphene quantum dots assisted exfoliation of atomically-thin 2D materials and as-formed 0D/2D van der Waals heterojunction for HER. *Carbon* **2021**, *184*, 554–561.
[27] Joyner, J.; Oliveira, E. F.; Yamaguchi, H.; Kato, K.; Vinod, S.; Galvao, D. S.; Salpekar, D.; Roy, S.; Martinez, U.; Tiwary, C. S. et al. Graphene supported $MoS_2$ structures with high defect density for an efficient HER electrocatalysts. *ACS Appl. Mater. Interfaces* **2020**, *12*, 12629–12638.
[28] Wang, S. H.; Wang, L. L.; Xie, L. B.; Zhao, W. W.; Liu, X.; Zhuang, Z. C.; Zhuang, Y. L.; Chen, J.; Liu, S. J.; Zhao, Q. Dislocation-strained $MoS_2$ nanosheets for high-efficiency hydrogen evolution reaction. *Nano Res.* **2022**, *15*, 4996–5003.
[29] Cordova, A.; Blanchard, P.; Lancelot, C.; Frémy, G.; Lamonier, C. Probing the nature of the active phase of molybdenum-supported catalysts for the direct synthesis of methylmercaptan from syngas and $H_2S$. *ACS Catal.* **2015**, *5*, 2966–2981.